

Nonlinear effects of phase blurring on Fourier transform holograms

Markus Duelli,* Li Ge, and Robert W. Cohn

The ElectroOptics Research Institute, University of Louisville, Louisville, Kentucky 40292

Received October 22, 1999; revised manuscript received May 1, 2000; accepted May 8, 2000

Liquid-crystal light valves can have intensity-dependent resolution. We find for a nematic liquid-crystal light valve that this effect is well modeled as a phase that has been blurred by a linear space-invariant filter. The phase point-spread function is measured and is used in simulations to demonstrate that it introduces intermodulation products to the diffraction patterns of computer-generated Fourier transform holograms. Also, the influence of phase blurring on a pseudorandom-encoding algorithm is evaluated in closed form. This analysis applied to a spot array generator design indicates that nonlinear effects are negligible only if the diameter of the point-spread function is a small fraction of the pixel spacing. © 2000 Optical Society of America [S0740-3232(00)01608-2]

OCIS codes: 230.6120, 070.2580, 030.6600, 160.3710, 100.3020.

1. INTRODUCTION

Loss of spatial resolution in a linear space-invariant imaging system is determined by the convolution of the input image with the point spread function (PSF) of the system. That is, the PSF blurs the input image. Many spatial light modulators (SLM) also can be viewed as linear space-invariant systems that convert an input image into an output image. Image blurring from this transformation can also be ascribed to a device PSF (sometimes referred to as an influence function).

For liquid-crystal light valves (LCLV), resolution has been reported to depend on the input intensity.¹⁻⁴ For instance, we recently studied a LCLV that was quoted as having 40 line pairs/mm resolution for low illumination levels and 4 line pairs/mm for high illumination levels.⁵ Thus a simple convolution model of resolution loss is not appropriate for LCLV's used as intensity displays. However, a convolution relationship appears to exist between input intensity images and output phase images. Specifically, in this paper we measure the phase PSF and find that, except for a scale factor, it is independent of the input intensity. Therefore phase blurring in LCLV's can be modeled by linear space-invariant filtering of the phase. The reason for the apparent loss in output resolution as a function of input intensity in Refs. 1-5 is not due to a loss in input phase (ϕ) resolution but rather to the nonlinear transformation from phase to the resulting complex-valued modulation [$\exp(j\phi)$].

In this study we specifically consider the nonlinear effects of phase blurring on phase-only LCLV's used to produce optical Fourier transforms. It is important to recognize that even if there is no phase blurring, the nonlinear transform $\phi \rightarrow \exp(j\phi)$ is inherent in the design of phase-only computer-generated holograms. Various encoding techniques have been developed for which the Fourier transform of $\exp(j\phi)$ approximates the Fourier transform of a desired fully complex modulation $\mathbf{a}_c \equiv a_c \exp(j\psi)$.^{6,7} One such encoding method, pseudo-

random encoding,^{5,8-11} (PRE), approximates the desired modulation in an average sense (which is reviewed in Subsection 4.A). Here we note that this approximate mapping from the desired signal \mathbf{a}_c to the encoded phase-only signal $\exp(j\phi)$ can be viewed as a linear (or more precisely, a quasi-linear) space-invariant system. In this way encoding approximately linearizes a nonlinear system.

This quasi-linear relationship found for encoding algorithms can be destroyed by phase blurring. The simplest model necessary to show that phase blurring is a nonlinear effect is to convolve the phase $\phi(x)$ that is a function of spatial coordinate x with the single-lag filter function (or phase PSF)

$$h(x) = (1 - \alpha)\delta(x) + \alpha\delta(x - \Delta), \quad (1)$$

where $\delta(x)$ is the Dirac delta function, Δ is a spatial offset, and α is a weighting coefficient between 0 and 1. The frequency response of the blurred phase is the frequency response of the phase multiplied by the frequency response of the PSF. However, the complex-valued modulation becomes

$$\begin{aligned} \exp[j\phi(x)*h(x)] &= \exp[j\phi(x)] \\ &\times \exp\{j\alpha[\phi(x - \Delta) - \phi(x)]\}, \quad (2) \end{aligned}$$

and its Fourier transform contains the encoded spectrum of $\exp(j\phi)$ convolved, rather than multiplied, by the spectrum of $\exp\{j\alpha[\phi(x - \Delta) - \phi(x)]\}$. This additional term is responsible for errors in the intensities of the desired Fraunhofer diffraction pattern at the design frequencies and for noticeable unwanted diffraction orders at the other frequencies. Therefore phase blurring introduces nonlinear effects into the complex-valued modulation and the resulting Fraunhofer diffraction pattern. In Sections 4 and 5 we will use the single-lag blur model of Eq. (1) in modeling and experimental demonstrations of the blurring effect. This model is especially well suited for ex-

perimental implementation of blurring with a pixelated, electrically addressed SLM that is reported in Section 5.

Phase blurring also bears some resemblance to the problem of phase scaling errors in computer-generated holograms (CGH's). This can be seen by rewriting Eq. (2) as

$$\exp[j\phi(x)*h(x)] = \exp[j(1 - \alpha)\phi(x)]\exp[j\alpha\phi(x - \Delta)]. \quad (3)$$

The term $\exp[j(1 - \alpha)\phi(x)]$ has scaled phase, which is known to reduce diffraction efficiency and for off-axis holograms introduces an on-axis component.^{7,12,13}

Unwanted diffraction orders arising from a phase-blurred LCLV have been experimentally observed for both PRE and a nonrandom phase-only encoding algorithm.⁹ In Ref. 9 and earlier studies, while we were aware of a spatial-frequency-dependent loss of phase range, we did not model this as phase blurring, nor did we consider the related nonlinear effects on the diffraction pattern.^{5,8,9} Instead, we attempted to minimize phase blurring by making the pixel spacing of the discretely sampled CGH's large with respect to the maximum phase slope anticipated. At the time, the major source of errors between the experimentally measured and the simulated results was assumed to be various point nonlinearities—e.g., the inaccurate setting of the mapping between input intensity and phase, variations in response across the SLM, and quantized phase levels. However, in this study we find that even a small amount of blurring can be quite noticeable. For the spot array generator designs considered in this paper, we find that the diameter of the phase PSF needs to be a quite small fraction of the pixel spacing for the nonlinear effects of blurring to be negligible.

The phase-blurring paradigm provides a unified view of SLM spatial properties that have been characterized in terms of spatial-frequency-dependent phase (Fig. 4 of Ref. 8), diffraction efficiency (Refs. 1, 2, 4, 14, and Fig. 5 of Ref. 8), and effective complex amplitude [Fig. 11(b) of Ref. 5]. Phase-blurring models have an added advantage in that they can be used to model distortion in phase-only holograms that consist of a multitude of spatial frequencies rather than a single spatial frequency.

In this paper we demonstrate through a combination of measurements and simulations that phase-only LCLV's are reasonably well described by a space-invariant phase-blurring model, and we quantify the magnitude of the effect on Fourier transform holograms designed by PRE. We also introduce blurring into an electrically addressed SLM and evaluate the performance as a function of the degree of blurring. Although phase blurring affects all encoding algorithms, we focus on PRE because the effects of phase blurring on PRE can be analyzed in closed form. Such an expression is derived for the case of single-lag blurring and is used to evaluate the distortion of the far-field pattern from a PRE designed spot array generator. The expression is also used to consider the possibility of predistorting the phase so as to compensate for blurring.

2. ILLUSTRATION OF THE EFFECTS OF PHASE BLURRING

The effects of phase blurring on Fourier transform holograms are illustrated in Fig. 1 for the comparison of a spot array generator that does not suffer from phase blurring [Fig. 1(a)] with one that does [Fig. 1(b)]. For diffractive optical elements (DOE's) that have abrupt transitions between pixels, blurring should not be an issue. For example, Fig. 1(a) shows the far-field intensity pattern (for an 850-nm illumination source) of an eight-phase-level transmissive DOE that was designed by a specific blended PRE algorithm.^{10,15} The device consists of 300×300 square pixels. Each pixel is $13.3 \mu\text{m}$ on a side, and the sidewalls are essentially vertical except for some ledges that are due to misalignment errors between successive mask layers. (The ledges, as measured with an atomic force microscope are never larger than $0.4 \mu\text{m}$). The diffractive optic is designed to produce an 8×8 array of equally spaced spots off axis. One unit spacing to the right and one unit below the spot array is a faint spot located on the optical axis. Additional features are the sidelobes between the spots. These are due to the small number of repetitions (4×4) of the 75×75 pixel unit cell in the spot array design function. Finally, there is a background pattern of speckle that is an essential byproduct of the PRE algorithm. There are no other noticeable

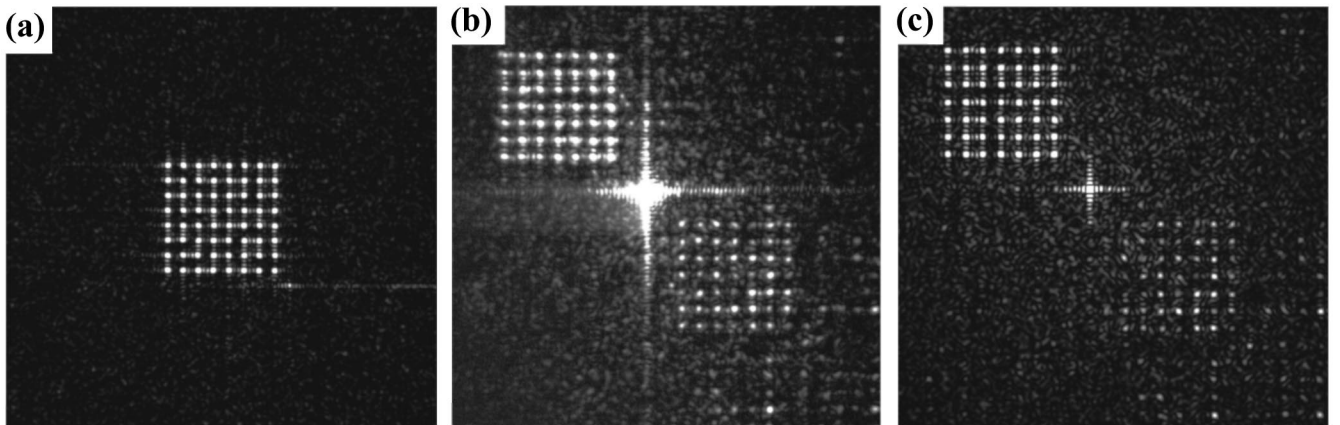


Fig. 1. Far-field diffraction patterns from (a) a DOE, (b) a LCLV, and (c) a simulation of (b) that includes a linear shift-invariant phase-blurring model. Maximum white in the gray-scale images correspond in (a) and (c) to 30% and in (b) to 20% of the average of the peak intensities of the spots in the desired spot array.

Table 1. Performance of PRE Implemented on a DOE

Metric	Theory	Experiment
SNR	916	942
SPR	35	52
NU ^a (%)	8.2	8.3
η (%)	38	41

^aThe experimental result for NU is the average for seven devices measured with the procedure described in Ref. 16. The standard deviation of NU is 0.8%.

Table 2. Performance of PRE Implemented on a LCLV

Metric	Ideal (No Blurring)	Simulated Phase Blurring	Experi- mental Results	Prefiltering and Blurring
SNR	254	148	73	340
SPR	17	3	1.9	18
NU (%)	10	27	33	18
η (%)	43	31	—	49
E_0/E_1 (%)	0	59	—	2
E_{-1}/E_1 (%)	0	15	36	0

features between the optical axis and the (1,1) grating order (corresponding to the spatial frequency that is the reciprocal of the pixel pitch).

Figure 1(b) shows a 7×7 spot array from a Hughes LCLV (nematic, parallel aligned). The modulation pattern consists of a 128×128 pixel image designed by PRE. The modulation values are identical to those reported in Ref. 9. The modulation is generated by projecting a gray-scale image from a red phosphor CRT onto the write side of the LCLV. The CRT is driven by the signal from a computer video display card set to a resolution of 800×600 pixels and a frequency of 56 Hz. A subimage of 384×384 video pixels is imaged into a $19.2\text{-mm} \times 19.2\text{-mm}$ area of the LCLV. Each modulation pixel corresponds to 3×3 video pixels or $150 \mu\text{m} \times 150 \mu\text{m}$. The modulation pattern is read out in phase-only mode by reflecting a linearly polarized 488-nm laser beam off the read side of the SLM. Additional information on the optical setup and the LCLV characteristics are described in Refs. 5 and 9.

Many of the same features as in Fig. 1(a) are seen in Fig. 1(b). Note that the pattern in Fig. 1(b) has a higher level of background speckle than that in Fig. 1(a), but this is due to the smaller number of pixels in the PRE design. The main differences between the two patterns are that in Fig. 1(b) there are a relatively intense on-axis spot, a faint mirror image, and an additional pattern of spots to the right and below the mirror image. If the spot array is designed centered on axis, these patterns are coincident, and if the spot array is further off axis, the patterns can be separated into nonoverlapping diffraction orders (which is discussed further in Subsection 5.D).

The simulated performance of the 8×8 spot array in Table 1 and of the 7×7 spot array in the first column of Table 2 are somewhat comparable in terms of diffraction efficiency (η), signal-to-noise ratio (SNR), signal-to-peak-

noise ratio (SPR) and nonuniformity (NU). (See Appendix A for a review and definition of these metrics.) In Table 1 the experimentally measured performance of the glass diffractive optic is comparable to the simulated performance. However, in Table 2 the measured performance is substantially different and degraded for the design that is implemented on the LCLV. The performance change appears to be due in large part to the phase PSF of the LCLV, as is considered in the next section.

3. EVALUATION OF PHASE BLURRING AND ITS INFLUENCE ON PERFORMANCE

We evaluated the effect of the phase PSF by convolving the experimentally measured PSF with the desired phase. We first measure the PSF by focusing a He-Ne laser beam onto the write side of the LCLV device using a $6\times$ microscope objective. The waist diameter of the Gaussian beam is $11.1 \mu\text{m}$ full width at half-maximum (FWHM, or $32 \mu\text{m}$ at the e^{-2} intensity level). The LCLV pattern is read out as in Section 2 with a 488-nm wavelength. The beam is interfered with a reference wave front in a Michelson interferometer. The interferogram is recorded on a CCD camera for various write beam powers between 1.3 and $6.8 \mu\text{W}$, corresponding to peak phase shifts between 0.3π and 2π . The phase profile for each image is calculated by point-by-point conversion from the intensity to phase. For each resulting image the phase profile is approximately a circular Gaussian with a diameter of $54 \mu\text{m}$ FWHM. (For comparison, the interferogram intensity pattern has a diameter of $72 \mu\text{m}$ FWHM when the peak phase shift is π .) The unchanging shape of the phase profile indicates that the phase profile corresponds to the phase PSF and that phase blurring for the LCLV is reasonably modeled by linear space-invariant filtering.

We also verified that the divergence of the write beam through the photodetecting layer of the LCLV does not significantly contribute to blurring. This was demonstrated by observing that the interferogram remains unchanged when the waist position is translated several millimeters along the optical axis. [Note that the theoretical depth of focus (range over which the waist expands less than a factor of $1.41\times$) is 2.54 mm .] These results show that the width of the phase PSF is nearly that of the $150\text{-}\mu\text{m}$ modulation pixels used for the experiments in Section 2.

While these experiments demonstrate the presence of phase blurring of the LCLV, they do not include the additional sources of resolution loss from the video card, the CRT, and the imaging system that are part of the complete SLM system described in Section 2. For this reason the phase PSF also is measured for the entire system with a single video pixel used as our closest approximation to a point source. The geometric image of this pixel (based on a $1.9\times$ demagnification between the CRT and the LCLV) would be $50 \mu\text{m} \times 50 \mu\text{m}$. The resulting phase image is once again observed to be approximately circular Gaussian but with a somewhat larger diameter of $59.4 \mu\text{m}$ FWHM. In our computer simulations we use this phase pattern as an approximation of the phase PSF of the SLM system.

The effect of blurring is evaluated by convolving the measured PSF with the desired phase modulation and then Fourier transforming the blurred modulation. This is done by digital simulation in which the PSF and the designed modulation are sampled every $37.5 \mu\text{m}$ in the x and y directions corresponding to a sample spacing that is one fourth the modulation pixel spacing $\Delta = 150 \mu\text{m}$. A 7×7 array of samples is used to represent the phase PSF. Sample values outside the 7×7 array are rather small and are treated as zero in the simulations. Note that the sample values are normalized so that they add up to unity and thus reproduce the desired phase when convolved with a constant phase image. The complex modulation is calculated from the resulting blurred phase. This is zero padded to produce 2048×2048 sample points, and then the simulated diffraction pattern is calculated with the fast Fourier transform (FFT).

This procedure was used to model the experimental results that are shown in Fig. 1(b). Using the same designed modulation in the simulation procedure gives the diffraction pattern of Fig. 1(c). The location and relative strengths of the unwanted diffraction orders appear to the eye to be quite similar. The major disagreement is that the actual on-axis spot is much brighter than the simulated spot. This is due to reflections from the cover glass of the LCLV, which is not incorporated into the models. The second and third columns of Table 2 compare three performance measures of the simulated and measured spot arrays. For each measure the experimental performance is lower than for the simulated performance. However, these values compare much more closely than they do with the values for the spot array that is unaffected by blurring (first column of Table 2). We have repeated these comparisons for a number of designs and encoding algorithms, and we observe similar trends in each case. Thus we believe that these results indicate that blurring is a major contributor to the loss of performance.

To gain additional information on the effect of phase blurring, we repeated the simulations with PSF's of various diameters between 6 and $90 \mu\text{m}$. The same measured PSF as above is used except that it is resampled and scaled to the corresponding diameter. The sample spacing (for both the PSF and modulation) is also reduced from one fourth to one eighth of the modulation pixel spacing Δ to permit adequate sampling of the smaller-diameter PSF's. For reasons of numerical efficiency the PSF kernel is limited to an 11×11 array of samples. For scalings of the PSF to large diameters the truncation of the tails of the PSF will lead to an underestimation of the effects of blurring, and for very large diameters the curves eventually flatten out as a result of the truncated PSF approaching a rect function. Even for $\Delta_{\text{PSF}}/\Delta = 0.396$ the spatial extent of the kernel is somewhat shorter than the kernel used for the simulated results in Table 2. This leads to NU and E_0/E_1 being somewhat smaller in Fig. 2 than in Table 2. However, the discussion of the Fig. 2 results will focus on the smaller values of $\Delta_{\text{PSF}}/\Delta$ for which the truncation effect is even less significant.

Figure 2 summarizes the results of these simulations for two performance measures: The relative energy in

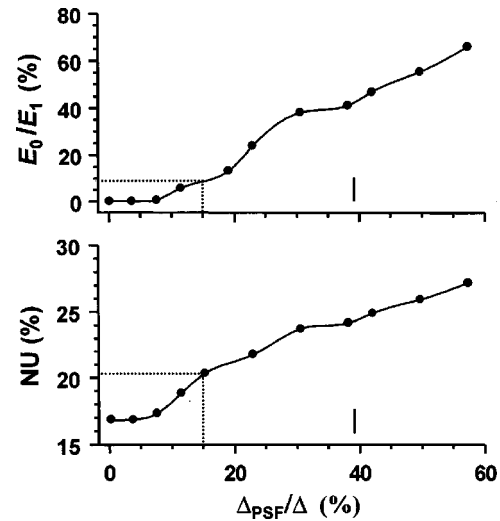


Fig. 2. Simulated effect of phase blurring on performance for phase PSF's of various diameters. The vertical bars indicate the value of $\Delta_{\text{PSF}}/\Delta$ corresponding to the phase PSF measured for the actual LCLV. The dotted lines indicate the performance values for $\Delta_{\text{PSF}}/\Delta = 0.15$.

the on-axis spot relative to the resulting spot array (E_0/E_1) and NU of the spot array. These are plotted as a function of PSF diameter relative to pixel spacing ($\Delta_{\text{PSF}}/\Delta$). The top plot in Fig. 2 shows that an increasing fraction of the energy appears in the on-axis spot with increased blurring. For a relative PSF diameter of only 15%, the energy in the on-axis spot is 10% of the energy in the spot array, or, equivalently, $\sim 5\times$ brighter than the average spot in the 49-spot array. The bottom plot in Fig. 2 shows that the spot array intensities become less uniform with increasing blur diameter. For a relative PSF diameter of 15%, NU has increased by 20% relative to NU for the ideal design. Even for this small degree of blurring, the changes to this design are quite significant. From these results we conclude that the spot array generator is surprisingly sensitive to a relatively small amount of blurring.

4. ANALYSIS OF PHASE BLURRING ON PSEUDORANDOM ENCODING

The results of Section 3 indicate that phase blurring can introduce undesirable and noticeable nonlinear effects. PRE algorithms,^{8,9,11} which approximate linear mappings between the desired complex modulation values and the modulation values that the SLM can actually produce, are subject to these nonlinear effects. The influence of a two-pixel (nearest-neighbor) blurring model on an encoding algorithm is analyzed in this section. In Section 5 this class of phase PSF's is implemented and experimentally studied with an electrically addressed SLM for which blurring is negligible. This permits a comparison of measured and simulated diffraction patterns for various degrees of blurring.

A. Derivation and Analysis of the Pseudorandom-Encoding Algorithm

The derivation of the blurring-induced distortion follows from the definitions and properties of PRE, which we re-

view. PRE algorithms for modulation-range-limited SLM's encode the desired complex modulation \mathbf{a}_{ci} at the i th SLM pixel in the average sense,

$$\mathbf{a}_{ci} = \int \mathbf{a} p_i(\mathbf{a}) d\mathbf{a} \equiv \langle \mathbf{a} \rangle_i, \quad (4)$$

where $p_i(\mathbf{a})$ is the probability density function (PDF) of the SLM modulation \mathbf{a} that is a random variable and $\langle \cdot \rangle$ is defined as the ensemble-average operator. The encoding algorithm is designed by finding a PDF that satisfies the integral equation Eq. (4). For phase-only SLM's for which $\mathbf{a}_i = \exp(j\phi_i)$, Eq. (4) simplifies to

$$\mathbf{a}_{ci} = \int \exp(j\phi) p_i(\phi) d\phi = \langle \exp(j\phi) \rangle_i. \quad (5)$$

This can be satisfied by a variety of PDF's as long as the magnitude of the desired complex modulation \mathbf{a}_{ci} is less than unity.¹⁶

A PRE algorithm that is amenable to analysis of phase blurring is based on the binary-phase random variable

$$\phi_i = \begin{cases} \psi_i - \nu_i/2, & 0 \leq s_i < 1/2 \\ \psi_i + \nu_i/2, & 1/2 < s_i \leq 1 \end{cases} \quad (6)$$

where $\psi_i = \arg(\mathbf{a}_{ci})$ is the phase of the desired complex modulation, $\nu_i/2$ is a random binary-phase offset, and s_i is a uniform random variable between 0 and 1. The PDF for the phase random variable in Eq. (6) is then written as

$$p_i(\phi) = \frac{1}{2} \{ \delta[\phi - (\psi_i - \nu_i/2)] + \delta[\phi - (\psi_i + \nu_i/2)] \}, \quad (7)$$

where $\delta(\phi)$ is the Dirac delta function. Evaluating the expected complex value of Eq. (5) with Eq. (7) gives

$$\langle \mathbf{a} \rangle_i = \cos(\nu_i/2) \exp(j\psi_i). \quad (8)$$

If the value of phase offset is set to

$$\nu_i/2 = \arccos(|\mathbf{a}_{ci}|), \quad (9)$$

then the result sought for Eq. (4), $\mathbf{a}_{ci} = \langle \mathbf{a} \rangle_i$, is obtained. This result leads to an encoding formula in which the magnitude of the random phase offset is set by using Eq. (9); and then, with use of Eq. (6), the sign of the phase offset is randomly selected according to the value of the random number s_i . The offset is added to the desired encoded phase $\psi_i = \arg(\mathbf{a}_{ci})$ to produce the encoded phase ϕ_i . This process is repeated for each pixel of the N pixels of the SLM.

The resulting far-field diffraction pattern of the complex field is proportional to

$$\mathbf{A}(f_x) \equiv \sum_{i=1}^N \mathbf{a}_i \exp(-j2\pi i \Delta f_x), \quad (10)$$

which is the Fourier transform of an array of equally spaced point sources of pitch Δ . (For purposes of explanation, the modulation is described in only one dimension and the pixel apertures are considered to be infinitesimal in width.) The expected value of Eq. (10) gives the desired complex diffraction pattern,

$$\mathbf{A}_c(f_x) = \langle \mathbf{A}(f_x) \rangle = \sum_{i=1}^N \mathbf{a}_{ci} \exp(-j2\pi i \Delta f_x), \quad (11)$$

where $\mathbf{A}_{ci}(f_x)$ is the Fourier transform of the desired modulation. The far-field diffraction pattern of the encoded modulation is known to produce a noise-perturbed approximation to the diffraction pattern that would result from the desired complex-valued modulation \mathbf{a}_{ci} .¹¹ The presence of background noise is indicated in the expected intensity pattern:

$$\begin{aligned} \langle |\mathbf{A}(f_x)|^2 \rangle &= \sum_{i=1}^N \sum_{k=1}^N \langle \mathbf{a}_i \mathbf{a}_k^* \rangle \exp[-j2\pi(i-k)\Delta f_x] \\ &= |\mathbf{A}_c(f_x)|^2 + \sum_{i=1}^N (1 - |\mathbf{a}_{ci}|^2). \end{aligned} \quad (12)$$

The second equality identifies the desired power spectrum and an additional white background noise. This result follows for the specific condition that \mathbf{a}_i is statistically independent of \mathbf{a}_k for $i \neq k$. (Independence is imposed in the design of PRE algorithms to simplify their derivation and implementation. In fact, blurring introduces statistical dependence between the values of neighboring pixels, which complicates the expected intensity, as will be shown in Subsection 4.B.) In the first equality, if the terms $\langle |\mathbf{a}_i|^2 \rangle = 1$ were replaced with $|\langle \mathbf{a}_i \rangle|^2 \equiv |\mathbf{a}_{ci}|^2$, then Eq. (12) would equal $|\mathbf{A}_c(f_x)|^2$. This factorization has been performed to produce the second equality.

The single summation term in Eq. (12) corresponds to the average intensity level of white background noise in the diffraction pattern. The noise is observed in experiments and simulations to be a speckle pattern.^{8,11} The intensity of the noise pattern depends on the intensity of the desired modulation values \mathbf{a}_{ci} . The closer the values are to unity magnitude, the lower is the intensity of the noise pattern. This can be viewed as measuring the dissimilarity between the desired modulation and the modulation achievable with the particular SLM. For this reason we often refer to this term as the error signal.

The expectation of the squared intensity provides additional information: specifically, the statistical variations of the pattern. The expression is derived in Ref. 11. Analyses of this higher-order moment show that the magnitude of the error signal is closely related to the deviations between the desired and the resulting diffraction patterns.

B. Effect of Blurring on the Encoding Algorithm

The effect of blurring on the PRE algorithm of Subsection 4.A is derived under the assumption that the encoded phase ϕ_i is blurred by a discrete version of the blurring function of Eq. (1). The two-pixel influence function is chosen because (1) it is the simplest blurring function to evaluate theoretically, (2) it can be directly implemented with an available electrically addressed SLM, and (3) it introduces the basic nonlinear effects that would be produced by a more extended blurring function. Repeating the analysis of Subsection 4.A for a two-pixel blur function evaluates to an effective complex amplitude of

$$\begin{aligned}
\mathbf{b}_i &\equiv \langle \exp\{j[(1-\alpha)\phi_i + \alpha\phi_{i-1}]\} \rangle \\
&= \langle \exp[j(1-\alpha)\phi_i] \rangle \langle \exp(j\alpha\phi_{i-1}) \rangle \\
&= \cos[(1-\alpha)v_i/2] \cos(\alpha v_{i-1}/2) \\
&\quad \times \exp\{j[(1-\alpha)\psi_i + \alpha\psi_{i-1}]\}. \tag{13}
\end{aligned}$$

The second equality follows from the statistical independence of the random variables ϕ_i . Equation (13) reflects the distortion introduced into Eq. (8) by blurring. The desired phase ψ_i from Eq. (8) is filtered by Eq. (1) in Eq. (13). Also, the amplitude is distorted. The Fourier transform [see Eq. (11)] of the sequence in Eq. (13) produces $\mathbf{B}(f_x)$, which is the expected complex diffraction pattern. The expected intensity diffraction pattern due to blurring is derived following a factorization procedure similar to that used to derive Eq. (12). In this case statistical dependencies exist between \mathbf{a}_i and \mathbf{a}_k for $k = i$, $k = i + 1$ and $k = i - 1$. Taking these conditions into account, the expected intensity patterns can be arranged as

$$\begin{aligned}
\langle |\mathbf{A}(f_x)|^2 \rangle &= |\mathbf{B}(f_x)|^2 + \sum_{i=1}^N (1 - |\mathbf{b}_i|^2) \\
&\quad + 2 \sum_{i=1}^{N-1} \text{Re}(\langle \exp[j(1-2\alpha)\phi_i] \rangle \langle \exp[-j(1-\alpha)\phi_{i+1}] \rangle \\
&\quad \times \langle \exp(j\alpha\phi_{i-1}) \rangle - \mathbf{b}_i \mathbf{b}_{i+1}^* \exp(j2\pi\Delta f_x)). \tag{14}
\end{aligned}$$

The second summation in Eq. (14) would be identically zero except for the term

$$\langle \exp[j(1-2\alpha)\phi_i] \rangle \neq \langle \exp[j(1-\alpha)\phi_i] \rangle \langle \exp[-j\alpha\phi_i] \rangle$$

that arises when terms $\langle \mathbf{a}_i \mathbf{a}_{i+1}^* \rangle$ are considered. Evaluation of the expectations in Eq. (14) using the PDF of Eq. (7) in Eq. (5), together with additional trigonometric identities, leads to

$$\begin{aligned}
\langle |\mathbf{A}(f_x)|^2 \rangle &= |\mathbf{B}(f_x)|^2 + \sum_{i=1}^N (1 - |\mathbf{b}_i|^2) + 2 \text{Re} \left\{ \sum_{i=1}^N \tan[(1-\alpha)v_i/2] \right. \\
&\quad \left. \times \tan(\alpha v_i/2) \mathbf{b}_i \mathbf{b}_{i+1}^* \exp(j2\pi\Delta f_x) \right\}. \tag{15}
\end{aligned}$$

Note that Eq. (15) is of the form

$$\langle |\mathbf{A}(f_x)|^2 \rangle = |\mathbf{B}(f_x)|^2 + C_1 + C_2 \cos(2\pi\Delta f_x + \Phi), \tag{16}$$

where C_1 represents the first summation in Eq. (15) and C_2 represents the magnitude of the second summation in Eq. (15). The second summation reduces to a single cosine component of phase shift Φ . Comparing Eq. (16) with Eq. (12) shows that the desired diffraction pattern $|\mathbf{A}_c(f_x)|^2$ is distorted into $|\mathbf{B}(f_x)|^2$, and the noise background changes from white to colored. It is interesting to note that, similarly to the summation term in Eq. (12), the white noise term C_1 indicates the amount of energy

scattered into the noise background.⁸ This result follows from the fact that the colored-noise term $C_2 \cos(2\pi\Delta f_x + \Phi)$ has a period of $1/\Delta$, which is the nonredundant bandwidth of the diffraction pattern. Thus this term integrates to zero energy over the bandwidth of any given diffraction order.

5. EVALUATION OF PERFORMANCE CHANGES DUE TO PHASE BLURRING OF PSEUDORANDOM ENCODING

The results and relationships derived in Section 4 are used to quantify performance changes as a function of the blurring parameter α . These computer-simulated results are compared with experimental results found with use of an electrically addressed SLM. The possibility of using predistortion to compensate for phase distortion is also considered in the simulations.

A. Simulation and Measurement of Nearest-Neighbor Blurring

The modulation pattern is designed to produce an off-axis array of 7×7 spots. Without blurring the modulation is identical to the one used with the LCLV in Sections 2 and 3. The modulation consists of 128×128 pixels complex modulation encoded to phase by the PRE method of Subsection 4.A. The encoded phase is then blurred along the diagonal direction so that the blurred phase is $(1-\alpha)\phi_{i,j} + \alpha\phi_{i-1,i-1}$. The resulting complex modulation pattern is then zero padded to produce a 512×512 array of samples. The sample array is then Fourier transformed by the FFT. A resulting intensity image is shown in Figs. 3(a) and 3(b) without and with blurring, respectively. The location of the various spots makes it qualitatively similar to the simulated image in Fig. 1(c). Metrics for various degrees of blurring (thick curves) are presented in Fig. 4. For $\alpha = 0.2$ there is substantial loss of performance in NU, and for the other two metrics the performance is substantially reduced for α as small as 0.1.

The simulated far-field intensity pattern resulting from this analysis is compared with measured intensity patterns from an electrically addressed SLM that is programmed to produce the identical blurred phase. The SLM used is a 128×128 pixel nematic liquid-crystal SLM from Boulder Nonlinear Systems (BNS). Additional technical specifications and experimental measurements of the device are presented in Ref. 10. One key property of this SLM is that intensity and interferometric images of the SLM indicate no noticeable coupling between nearest-neighbor pixels. Apparently the grounding electrodes between the pixels significantly reduce fringing fields compared with those found in the LCLV. As with the LCLV, the on-axis light is usually much brighter than the spot array. This is due not to blurring but rather to the relatively large percentage of light that is reflected from the cover glass of the SLM.

The experimental diffraction patterns produced for no blurring and for blurring ($\alpha = 0.5$) are presented in Figs. 3(d) and 3(e), respectively. Except for the on-axis spot that is due to reflections from the cover glass, these diffraction patterns are qualitatively similar to the simu-

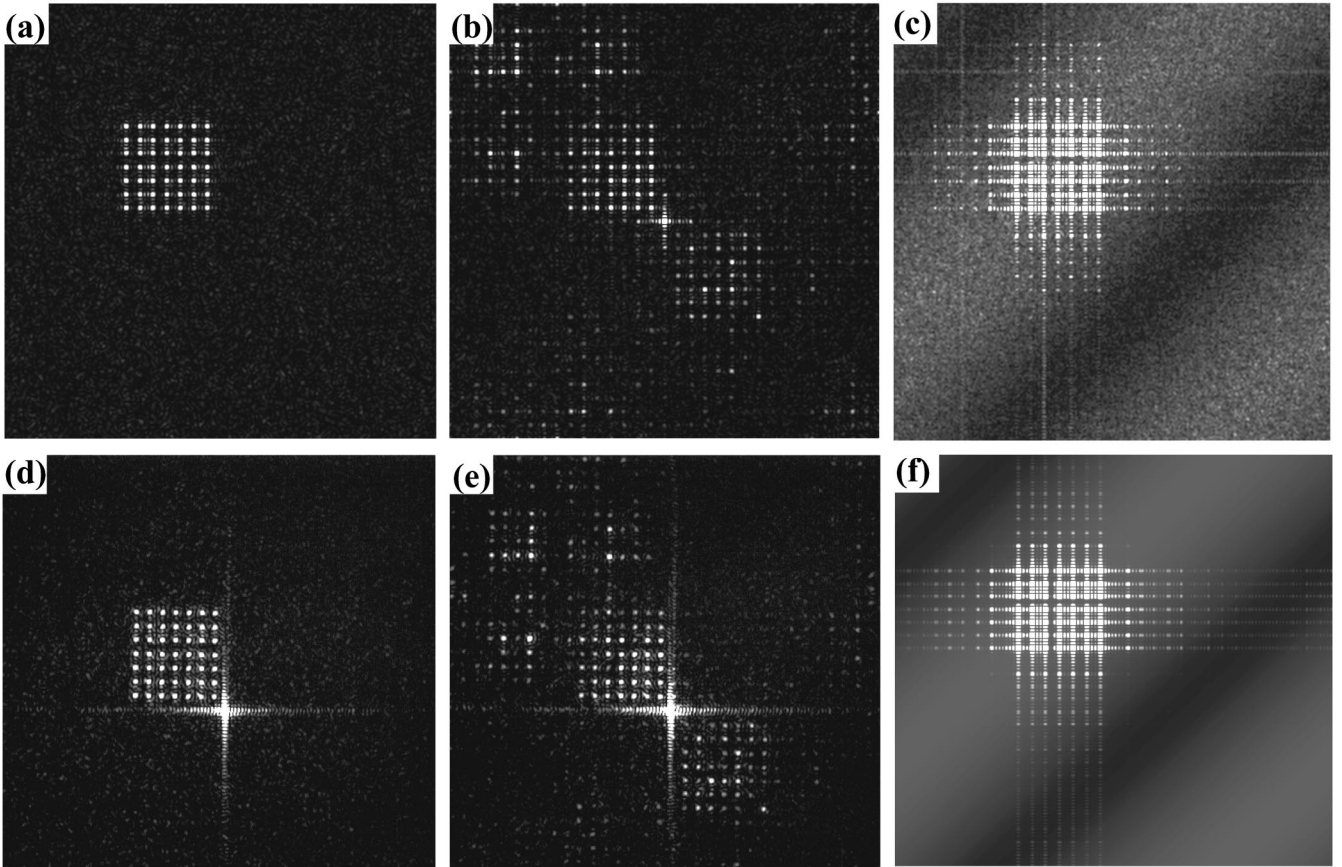


Fig. 3. Far-field diffraction patterns resulting from the identical PRE design of a spot array generator: (a) and (d) without phase blurring, (b) and (e) with phase blurring $\alpha = 0.5$, and (c) and (f) with phase blurring of a predistorted phase for $\alpha = 0.5$. (a) and (b) are simulated, (c) is the average of ten simulations each using a different random sequence for PRE, (d) and (e) are as measured for the BNS SLM, and (f) is the expected far-field intensity pattern as calculated with Eq. (15). Maximum white in the gray-scale images corresponds in (a) and (d) to 30%, in (b) and (e) to 50%, and in (c) and (f) to 1% of the average peak intensity of the desired spot array.

lated patterns in Figs. 3(a) and 3(b). The metrics calculated from the SLM diffraction patterns are plotted as dots in Fig. 4. Considering the inaccuracies in programming coherent SLM's and in measuring coherent optical patterns, the experimental diffraction patterns produce performance metrics that are reasonably similar to the simulated performance metrics. For SPR in Fig. 4 the discrepancy is quite noticeable for $\alpha < 0.06$. In this range the brightest noise spot is due to speckle noise. However, for larger values of α the peak noise is from peaks in the first harmonic of the spot array. (The on-axis spot is omitted from consideration in both experimental and simulated SPR, as discussed further in Appendix A.) The experimental measurements suggest that speckle noise is higher in practice than for the simulations. The higher speckle noise accounts in part for the measured values of NU being higher than the simulated values. Another influence on NU could be multiple coherent reflections between the SLM and its cover glass.¹⁷ The magnitude of the discrepancy between NU as measured and as simulated is in line with previous measurements of NU.^{10,17} Also, for small values of α the denominator term E_{-1} of E_1/E_{-1} is dominated by speckle noise. Thus in this range E_1/E_{-1} measures the SNR in the vicinity of the mirror (i.e., the -1) order.

Figure 4 also shows that a slight degree of blurring can improve individual metrics. This is not unreasonable.

For example, introducing (even a small degree of) phase blurring into a diffuser is known to convert its far-field intensity statistics from exponentially distributed into a modified Rician, which is much less likely to produce as large a maximum-intensity peak as does the exponential.⁵

B. Simulated Correction of Blurring by Predistortion of Phase and Limitations

The effect of phase blurring can be compensated by convolving the encoded phase modulation ϕ_i with the inverse filter h_i^{-1} . The inverse filter is defined such that convolving h_i with its inverse produces the delta function ($h_i * h_i^{-1} = \delta_i$). Therefore it is possible to numerically compensate the phase by first predistorting phase ($h_i^{-1} * \phi_i$) and then blurring it ($h_i * h_i^{-1} * \phi_i = \phi_i$). For the discretely sampled SLM with a phase PSF that is a discrete version of Eq. (1), $h_i = (1 - \alpha)\delta_i + \alpha\delta_{i-1}$, the inverse filter is known to be

$$h_i^{-1} = \frac{1}{1 - \alpha} \left(\frac{-\alpha}{1 - \alpha} \right)^i; \quad i \geq 0. \quad (17)$$

This filter is stable for $\alpha < 0.5$ and marginally stable for $\alpha = 0.5$. For $1 > \alpha > 0.5$ the data can be filtered in the reverse (anticausal) direction to ensure a numerically stable solution.^{18,19} It is clear from this discussion that the pre-

distorted phase can be exactly compensated by the inverse filter in Eq. (17) in a numerical simulation.

However, there is a practical limitation to using predistortion that can be seen by examining Eq. (17). The problem is that the predistorted phase range can be much greater than 2π . This can be appreciated by convolving the inverse filter with a step function of height 2π . For $\alpha = 0.5$ the sequence of predistorted phases is $[4\pi, 0, 4\pi, 0, \dots]$, and for $\alpha = 0.3$ the predistorted phase sequence is $[2.8\pi, 1.64\pi, 2.16\pi, 1.94\pi, \dots]$. The predistorted phase range is even greater for the PRE-designed 7×7 spot array generator. We find that the total phase range is 96π for $\alpha = 0.5$, 7.6π for $\alpha = 0.45$, and 5.8π for $\alpha = 0.3$. Since LCLV's are limited in phase range to near 2π (for practical reasons) it is likely that they will not be able to respond to predistorted addressing signals corresponding to phase shifts that are greatly in excess of 2π . Also, modding of the predistorted phase into the 2π range of the LCLV is not an acceptable option, and it will not correctly compensate for phase blurring.

There is also a limitation to using a blur-free, electrically addressed SLM to demonstrate phase compensation experimentally. Since the phase is both blurred and predistorted in the attached computer, the signal applied to the SLM is exactly the same signal as would have been applied to the SLM if there were no phase blurring.

Examination of Eq. (13) suggests that one could apply the inverse filter to the desired phase ψ_i , which also is

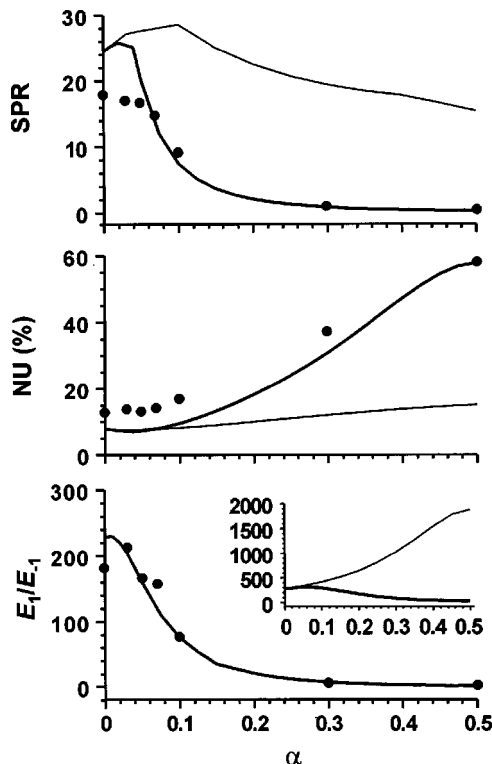


Fig. 4. Performance of PRE as a function of α , the degree of phase blurring. Solid curves report the computer-simulated results for the effect of phase blurring. Dots show the experimentally measured values obtained with the BNS SLM. Thin curves report the simulated performance if the phase is first predistorted through the inverse filter of Eq. (17). The inset plots E_1/E_{-1} over an extended range that shows the simulated performance for phase blurring and for phase blurring of the predistorted phase.

blurred by the single-lag phase PSF. Various simulations indicate that this phase distortion contributes to the appearance of undesired diffraction orders to a much greater degree than do the amplitude distortions of Eq. (13). While both amplitude and phase distortions can be exactly compensated for by predistorting ϕ_i , it is interesting to consider to what degree that predistortion of the desired phase ψ_i reduces the effects of blurring. The resulting far-field patterns are shown in Figs. 3(c) and 3(f). The performance in Fig. 4 for predistorted phase (thin curves) is generally better than for phase that is not predistorted (thick curves). For SPR and NU the performance is close to that for the original design (i.e., for $\alpha = 0$). The metric E_1/E_{-1} (inset in Fig. 4) is much larger after predistortion of the phase. This change is due to the following: (1) The contribution to E_{-1} from harmonics is negligible, as can be evaluated from the first term of Eq. (16). (2) Essentially only the speckle pattern contributes energy to E_{-1} . (3) The speckle pattern intensity is weakest in the region of the -1 order, and it is much weaker than for the case of no predistortion. For example, for $\alpha = 0.5$, C_1 , and C_2 in Eq. (16) are of similar magnitude for the predistorted design, and the -1 order is located in a region where the cosine term subtracts from and nearly cancels C_1 . The cosine variation of the speckle noise can be seen both for the simulated [Fig. 3(c)] and for the theoretical [Fig. 3(f)] expected intensity pattern. Specifically, the simulated expectation is the average of ten realizations of the identical PRE design, each using a different uncorrelated realization of the random sequence s_i , and the theory is the expectation from Eq. (15). The average of several realizations makes it easier to see and compare low-level features with the theory than does a single realization.

Two interesting results come out of this simulation. First, the compensation of the desired phase ψ_i in Eq. (13) results in values of NU and SPR that are close to the values for no phase blurring. Second, the compensated diffraction patterns appear very similar to the diffraction pattern without blurring. The main difference is that the speckle pattern in the compensated diffraction pattern [Figs. 3(c) and 3(f)] has a noticeable sinusoidal component ($C_2/C_1 \approx 0.6$, not just for $\alpha = 0.5$ but for $0.3 \leq \alpha \leq 0.5$), while the speckle pattern in diffraction patterns without blurring have no sinusoidal component, as indicated in Eq. (12). This is especially interesting because the sinusoidal component of speckle for the phase-blurred modulation in Figs. 3(b) and 3(e) is not apparent (since $C_2/C_1 < 0.01$).

Finding an exact inverse filter for a two-dimensional filter is nontrivial, and some approximation is usually required.^{18,19} For the 7×7 LCLV phase PSF measured in Section 3 we computed an approximate inverse by using the discrete Fourier transform to calculate the two-dimensional phase spectrum $H(f_x, f_y)$. The exact inverse filter is $H^{-1}(f_x, f_y)$. However, the function contains singularities. For this reason, amplitudes in excess of a threshold value γ are set to γ so that for $|H^{-1}| > \gamma$, the modified filter is $\gamma \exp[\arg(H^{-1})]$. We used the modified inverse filter to predistort the phase ϕ_i of the spot array generator design. We found through repeated experiments that a value of γ that is $25\times$ larger than the

minimum value of $|H^{-1}|$ reduces the effects of blurring on the performance metrics the most (as reported in the last column of Table 2). While predistortion of the blurred phase significantly corrects for blurring, approximations inherent in the inverse filter method do not completely restore the performance to the levels achieved if blurring were not present. As with the single-lag blurring function, the predistorted phase range (which is 40π) is too large to experimentally implement. Even for an isolated 2π step the predistorted phase range is 6.9π . Furthermore, owing to incomplete compensation, the phase range of the corrected step increases from 2π to 2.3π .

These results show that predistortion is numerically possible but physically quite difficult owing to the limited phase range of most LCLV's. These simulations do provide insight into the effect of blurring. In particular, the compensation of the desired phase ψ_i provides an example of a significant spatial variation of the speckle noise background. Also, these analyses show that modding of the phase into a 2π range, which often is taken for granted in CGH design, is not necessarily possible because of the nonlinearity inherent in phase blurring. This limitation is considered further in Subsections 5.C and 5.D.

C. Evaluation of Blurring on a Linear Phase Ramp

A standard method of evaluating phase distortion is to consider the effect on a single frequency f_0 .⁷ This corresponds to a desired phase that is a linear phase ramp or $\psi(x) = 2\pi f_0 x$. On the basis of current SLM's we also will assume that the phase is modded into a 2π range. The modded phase is a periodic function of period $1/f_0$. For the phase PSF of Eq. (1) the blurred phase over one period can be written as

$$\psi_b(x) = \begin{cases} 2\pi[(x - \alpha\Delta)f_0 + \alpha] & \text{if } 0 \leq x < \Delta \\ 2\pi(x - \alpha\Delta)f_0 & \text{if } \Delta \leq x < 1/f_0 \end{cases} \quad (18)$$

The blurred phase for $\Delta f_0 = 1/2$ and $\alpha = 1/3$ is plotted in Fig. 5. It can be seen that blurring reduces the phase range (thus introducing a dc component) and causes a phase discontinuity (thus producing higher-frequency components). The strengths of the desired and undesired diffraction orders are found by evaluating the integral

$$d_k = f_0 \int_0^{1/f_0} \exp[j\psi_b(x)] \exp[-j2\pi k f_0 x] dx, \quad (19)$$

which are the Fourier series coefficients of the complex modulation. The intensity of the diffraction orders evaluates to

$$|d_k|^2 = \begin{cases} (1 - \Delta f_0)^2 + (\Delta f_0)^2 + 2(\Delta f_0)(1 - \Delta f_0)\cos(2\pi\alpha) & \text{if } k = 1 \\ |[2/\pi(1 - k)]\sin[\pi\Delta f_0(1 - k)]\sin(\pi\alpha)|^2 & \text{if } k \neq 1 \end{cases} \quad (20)$$

Thus blurring applied to an ideal blazed grating introduces undesired diffraction orders at frequencies kf_0 , $k \neq 1$. However, if the linear phase were a continuous unmodded ramp, then the desired phase and blurred-phase patterns would both produce a single diffraction order at f_0 . The spots would be identical in intensity and differ only by a constant phase shift $2\pi\alpha\Delta f_0$.

The validity of Eq. (20) was compared with a computer simulation and experimental implementation with use of the BNS SLM. A comparison of the results for two values of α are summarized in Table 3. For the computer simulation the Fourier series coefficients are calculated by taking the FFT of one period of the blurred modulation.²⁰ One period in the simulation consists of 4.75Δ or, equivalently, $\Delta f_0 = 4/19$. Equation (20) and the simulation give nearly identical results, indicating that Eq. (20) is correct. This phase modulation also is programmed on the 128×128 pixel SLM. The simulated and experimental diffraction patterns are compared in Table 3. The results are reasonably similar to the theory in relative strength. This suggests that the SLM produces a phase modulation that is similar to the modded phase.

D. Comparison of the Phase-Ramp Model with the Pseudorandom-Encoding Model of Blurring

In this section we compare the effect of phase blurring on PRE as modeled in Eq. (15) with a traditional diffraction-efficiency model based on Eq. (20).

Models of periodic modulation similar to the one in Subsection 5.C have been widely used to predict the diffraction efficiency of DOE's. These models are based on the assumption that the desired diffraction pattern recon-

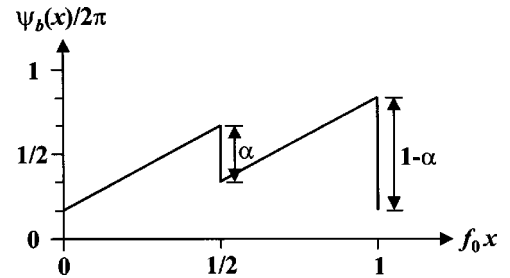


Fig. 5. Illustration of the distortion of a modded phase ramp of 2π range due to the phase PSF of Eq. (1).

Table 3. Diffraction-Order Intensities for a Modded Phase Ramp That Is Phase Blurred^a

Method of Analysis	I_{-1}	I_0	I_1	I_2	I_3
$\alpha = 0.3$					
Theory, Eq. (20)	0.106	0.165	1	0.165	0.106
Simulation	0.102	0.162	1	0.148	0.102
Experiment	0.150	—	1	0.136	0.212
$\alpha = 0.5$					
Theory, Eq. (20)	0.266	0.414	1	0.414	0.266
Simulation	0.256	0.405	1	0.368	0.253
Experiment	0.134	—	1	0.566	0.380

^aFor $\Delta f_0 = 4/19$. Data are normalized to I_1 . α is the degree of phase blurring.

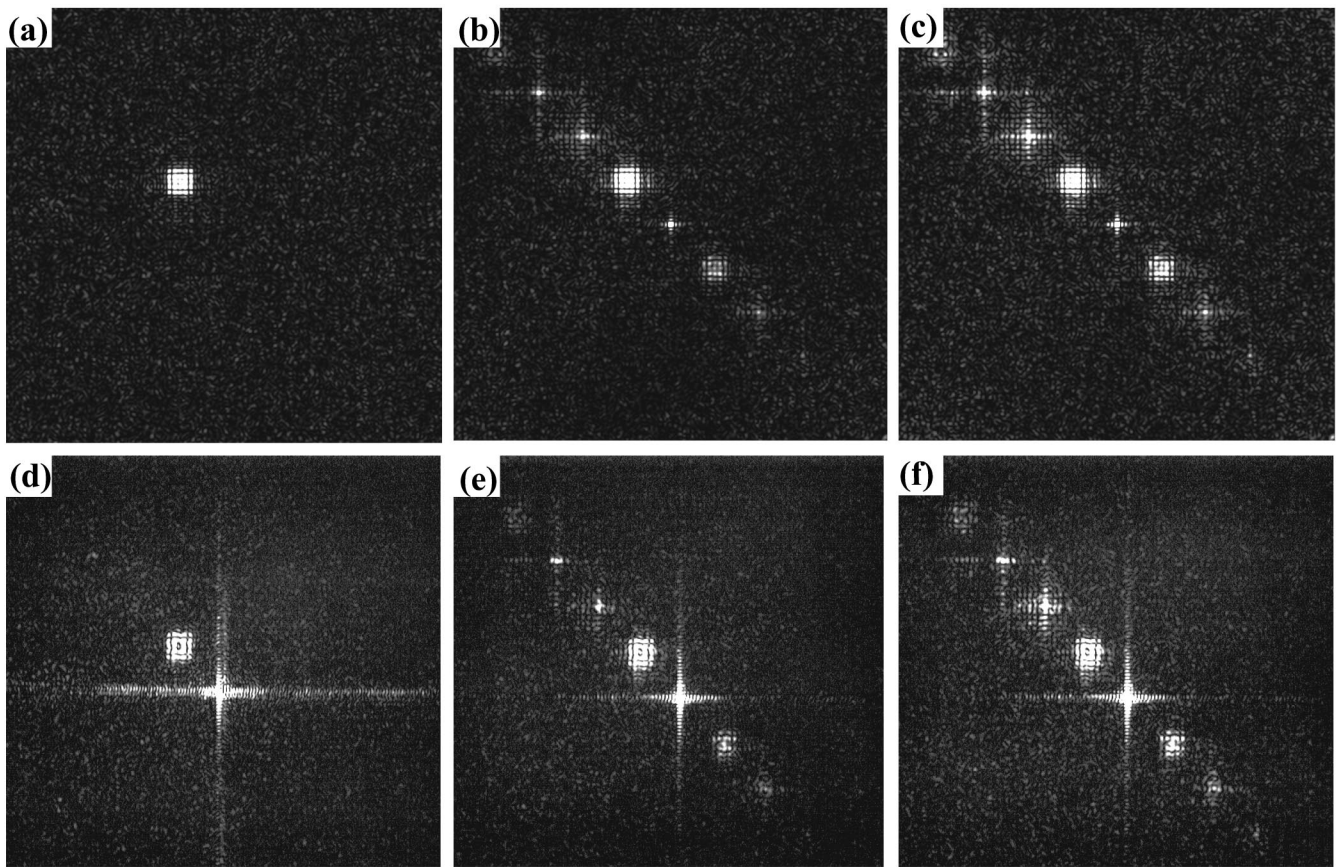


Fig. 6. Far-field diffraction patterns resulting from the identical PRE design of a spot array generator: (a) and (d) without phase blurring, (b) and (e) with phase blurring $\alpha = 0.3$, and (c) and (f) with phase blurring $\alpha = 0.5$. (a)–(c) are simulated, and (d)–(f) are as measured for the BNS SLM. Maximum white in the gray-scale images corresponds to 15% of the peak intensity level of the desired spot array.

Table 4. Diffraction-Order Intensities That Result from Phase Blurring of PRE^a

Method of Analysis	E_{-1}	E_0	E_1	E_2	E_3
$\alpha = 0.3$					
Eq. (20)	0.106	0.165	1	0.165	0.106
Theory, Eq. (15)	0.122	0.200	1	0.200	0.144
Simulation	0.127	0.211	1	0.202	0.146
Experiment	0.131	—	1	0.228	0.148
$\alpha = 0.5$					
Eq. (20)	0.266	0.414	1	0.414	0.266
Theory, Eq. (15)	0.278	0.455	1	0.416	0.305
Simulation	0.285	0.463	1	0.406	0.305
Experiment	0.258	—	1	0.555	0.284

^aFor $\Delta f_0 = 4/19$. Data are normalized to E_1 . α is the degree of phase blurring.

structs around a specific diffraction order. In this paper we have been considering the desired order to be the $k = 1$ order at spatial frequency f_0 . This center frequency can be viewed as the carrier frequency for the desired signal. In some cases (particularly if the modulation on the carrier has a small bandwidth and the modulation depth of the carrier is small) the diffraction efficiency for the modded linear phase ramp [found from

Eq. (20)] should correspond closely to the efficiency for the signal-modulated carrier. However, for the designs based on PRE (which ideally do not produce additional harmonics at kf_0 , $k \neq 1$) the bandwidth is greater than f_0 and the deviation between the phase ramp and the PRE phase modulation is frequently as large as $\pm\pi$.

To illustrate the differences between the two models we define a desired function that has a much smaller bandwidth. This is achieved by sampling the desired phase function for the 7×7 spot array generator more finely. The resulting function consists of 2×2 rather than 4×4 unit cells, and the spacing between the resulting spots is reduced by a factor of 1/2. A phase ramp is added to the desired modulation so that the spot array is centered $\Delta f_0 = 4/19$, the same frequency used in Subsection 5.C. The simulated diffraction pattern calculated from the 512×512 sample FFT of the blurred PRE design is shown in Figs. 6(a)–6(c). Compared with the previous design in Figs. 1 and 3, the desired diffraction pattern is much more separated from the harmonic patterns. However, there is still some overlap between the orders. Based on the shape of each order a unique and nonoverlapping window is chosen for performing the integration of intensity. The window for the 1 and -1 orders is chosen to be a cross-shaped area composed of two rectangles oriented at right angles to each other in x and y . Each rectangle is 33×65 samples. The window for the 0 and

3 orders is also a symmetric cross with arms in x and y . Each rectangle is 17×201 samples. The window for the 2 order is a rectangle that is 83×77 samples. Identical windows are applied to the simulation of the blurred PRE (i.e., the FFT of encoded modulation) and to the model [i.e., the expected intensity calculated from Eq. (15)]. The results are compared in Table 4 and are found to be nearly identical. These results do not compare quite as closely with the diffraction-order strengths calculated from Eq. (20). In particular, the intensities for Eq.(20) are symmetric around $k = 1$, whereas the energies calculated from Eq. (15) are not symmetric.

Perhaps even closer correspondence would be obtained if it were possible to further increase the carrier frequency and the separation between the orders. However, Eq. (15) accurately predicts the energy in a given window despite the overlap. Additionally, unlike Eq. (20), the simulations [Figs. 6(a)–6(c)] or Eq. (15) provide detailed intensity patterns around each harmonic frequency. Most of the same features seen in the simulations are also seen in Figs. 6(d)–6(f), which are the corresponding experimental diffraction patterns from the SLM. The measured values of energy E_k in Table 4 are somewhat closer to the theory with use of Eq. (15), with the greatest discrepancy ($\sim 25\%$) being for E_2 for $\alpha = 0.5$.

The model of blurring of PRE [Eq. (15)] appears to provide additional accuracy compared with the basic linear model of Eq. (20). The ability of the model to predict the detailed effects of blurring when the unwanted harmonic patterns overlap with the desired designs (such as in Fig. 3) is the key advantage of the blurred PRE model.

6. SUMMARY AND CONCLUSIONS

The historical approach of describing the resolution of LCLV's as a function of input level may not be the most appropriate for Fourier transform applications such as beam steering, pattern generation and matched filtering. The phase range desirable for these applications is near 2π and over this range the resolution of most LCLV's used as display devices changes dramatically. However, as measured for a specific LCLV, the phase resolution does not change noticeably, which suggests the suitability of the space-invariant phase-blurring model. Using the experimentally measured phase PSF in simulations produces far-field patterns with distortion products that are quite similar to those actually measured from the LCLV. Simulations in which the phase PSF is varied in diameter show that the blur diameter needs to be a very small fraction of the pixel spacing for the effects of blurring to be negligible for the 7×7 spot array generator design.

Additional experiments are performed with an electrically addressed SLM that has no appreciable coupling between nearest-neighbor pixels. Filtering of the electrical address signal is used to experimentally introduce various degrees of phase blurring. Performance is dramatically reduced for $\alpha = 0.1$, which, as with the LCLV experiments, indicates that a small degree of phase blurring can significantly alter performance. The effects of phase blurring on PRE designs can be compensated to a large extent by applying an inverse filter to the phase. How-

ever, this approach is not practical since it requires that the SLM have a phase range that greatly exceeds 2π .

A Fourier series analysis of a modded phase ramp subjected to phase blurring is performed to provide a clear example of the nonlinear generation of harmonics that is due to blurring. However, this result does not accurately predict the energy found in the diffraction orders of the PRE-designed spot array. Much more detailed information can be found from the closed-form expression Eq. (15) for the expected far-field intensity pattern. This expression predicts the distortion of each effective pixel value, which leads to the generation of undesired harmonics. It also predicts the expected noise power spectrum, which, owing to phase blurring, has a nonwhite distribution. Equation (15) is no more numerically efficient than numerical simulations involving the application of the PRE algorithm, blurring of the phase encoding, and calculation of the Fourier transform. However, the recognition that Eq. (15) is of the form of Eq. (16) provides insight into the nonlinear effects of phase blurring and a base from which to develop models of various performance metrics.

APPENDIX A

The definition and method of calculating the performance metrics used in this paper are collected here for easy reference. The metrics of signal-to-noise ratio (SNR), signal-to-peak-noise ratio (SPR), nonuniformity (NU), and diffraction efficiency (η) are reviewed from earlier work.^{5,8–10} Additional metrics that are useful for describing the nonlinear effects of blurring are the intensities I_k and the energies E_k of the k th diffraction order that result from blurring of the desired modulation.

The orders are defined so that $k = 0$ corresponds to light on the optical axis and $k = 1$ corresponds to the desired reconstruction centered at frequency f_0 . The energy in a spot array and its harmonic orders is compared as a ratio. A particular window of integration around each order is chosen to make a fair comparison between the values of E_k . The same window is used for comparing experiment, simulation, and theory. We present this data as a ratio of energies such as E_k/E_1 . For most measurements reported in all sections except Subsections 5.B and 5.D, we calculate E_1 so as to minimize energy contributions from speckle. This is accomplished by summing the intensities only at the centers of the 49 desired spots. The ratio E_{-1}/E_1 is calculated by summing the intensities at the same 49 frequencies, appropriately centered around the frequency $-f_0$. Modified windows are used to minimize the variability of speckle from the -1 order and the overlap between harmonics. These windows are specified in Subsections 5.B and 5.D, respectively.

In this paper the ratio of E_1 to either E_0 or E_{-1} is reported to show the production of unwanted orders by blurring. We do not report experimental measurements of E_1/E_0 , because reflections from the cover glass of both SLM's produce bright spots on the optical axis that are not accounted for in the theory and simulations. Rather than adjusting the theory to the specific modulators, we

chose to experimentally measure E_1/E_{-1} . For this same reason we do not report experimentally measured values of I_0 and η .

The SNR is the average spot intensity (specifically, $E_1/49$ for the 7×7 spot array) divided by the average noise intensity. The noise intensity is calculated from the two quadrants in the diffraction other than where the desired diffraction signal and its harmonics appear. The identical region is used for calculations from the simulations and the experiments. The SPR is the average spot intensity divided by the most intense noise peak found in the diffraction pattern. The on-axis spot and the side-lobes of the spots in the vicinity of the desired spot array are omitted from this calculation. However, spots from the harmonic orders are included in the calculation of SPR. The NU is the standard deviation of the desired spot intensities relative to the average spot intensity. The standard deviation and average are calculated from the peak intensities of the 49 spots located around f_0 . The diffraction efficiency values are reported here for purposes of making relative comparisons of energy distribution between desired and undesired portions of the light distribution. The value of η is calculated in the simulations by summing the energy in a window around the 7×7 spot array and dividing by the total energy of the FFT, which cover only the frequency range of the SLM grating order $1/\Delta$. Energy that appears in adjacent grating orders, which depends on the pixel aperture, is not considered in the theory or simulations of the diffraction patterns. As mentioned above, experimental measurements of diffraction efficiency are not reported because the presence of the reflection from the cover glass obscures the measurement of I_0 .

ACKNOWLEDGMENTS

This study was supported by U.S. Office of Naval Research grant N00014-96-1-1296 and NASA cooperative agreement NCC5-222. The diffractive optical elements were fabricated by Honeywell as part of the Defense Advance Research Projects Agency DOE foundry run.

*When the work was performed, the authors were with University of Louisville. M. Duelli's current address is Optical Coating Laboratory, Inc., 2789 Northpoint Parkway, MS 125-3, Santa Rosa, California 95407-7397.

Address correspondence to R. W. Cohn at the location on the title page or by e-mail: rwcohn@louisville.edu.

REFERENCES

1. D. Casasent, "Performance evaluation of spatial light modulators," *Appl. Opt.* **18**, 2445–2453 (1979).
2. A. D. Fisher and J. N. Lee, "The current status of two-dimensional spatial light modulator technology," in *Optical and Hybrid Computing*, H. H. Szu, ed., Proc. SPIE **634**, 352–371 (1986).
3. T. D. Hudson and D. A. Gregory, "Optically addressed spatial light modulators," *Opt. Laser Technol.* **23**, 297–302 (1991).
4. D. V. Wick, T. Martinez, M. V. Wood, J. M. Wilkes, M. T. Gruneisen, V. L. Berenberg, M. V. Vasil'ev, A. P. Onokhov, and L. A. Beresnev, "Deformed-helix ferroelectric liquid-crystal spatial light modulator that demonstrates high diffraction efficiency and 370-line pairs/mm resolution," *Appl. Opt.* **38**, 3798–3803 (1999).
5. R. W. Cohn, A. A. Vasiliev, W. Liu, and D. L. Hill, "Fully complex diffractive optics by means of patterned diffuser arrays: encoding concept and implications for fabrication," *J. Opt. Soc. Am. A* **14**, 1110–1123 (1997).
6. R. W. Cohn and L. G. Hassebrook, "Representations of fully complex functions on real-time spatial light modulators," in *Optical Information Processing*, F. T. S. Yu and S. Jutamulia, eds. (Cambridge U. Press, Cambridge, UK, 1998), Chap. 15, pp. 396–432.
7. W. J. Dallas, "Computer-generated holograms," in *The Computer in Optical Research*, B. R. Frieden, ed. (Springer-Verlag, Berlin, 1980), Chap. 6, pp. 291–366.
8. R. W. Cohn and M. Liang, "Pseudorandom phase-only encoding of real-time spatial light modulators," *Appl. Opt.* **35**, 2488–2497 (1996).
9. R. W. Cohn and M. Duelli, "Ternary pseudorandom encoding of Fourier transform holograms," *J. Opt. Soc. Am. A* **16**, 71–84; "errata," 1089–1090 (1999).
10. M. Duelli, M. Reece, and R. W. Cohn, "A modified minimum distance criterion for blended random and nonrandom encoding," *J. Opt. Soc. Am. A* **16**, 2425–2438 (1999).
11. R. W. Cohn and M. Liang, "Approximating fully complex spatial modulation with pseudorandom phase-only modulation," *Appl. Opt.* **33**, 4406–4415 (1994).
12. G. Paul-Hus and Y. Sheng, "Optical on-axis real-time phase-dominant correlator using liquid crystal television," *Opt. Eng.* **32**, 2165–2172 (1993).
13. R. W. Cohn and J. L. Horner, "Effects of systematic phase errors on phase-only correlation," *Appl. Opt.* **33**, 5432–5439 (1994).
14. E. Shafir, H. Bernstein, A. A. Friesem, and H. Grubel, "Method for measuring the spatial frequency response of phase-modulating spatial light modulators," *Opt. Eng.* **27**, 71–74 (1988).
15. L. G. Hassebrook, M. E. Lhamon, R. C. Daley, R. W. Cohn, and M. Liang, "Random phase encoding of composite fully-complex filters," *Opt. Lett.* **21**, 272–274 (1996).
16. R. W. Cohn, "Analyzing the encoding range of amplitude-phase coupled spatial light modulators," *Opt. Eng.* **38**, 361–367 (1999).
17. M. Duelli, D. L. Hill, and R. W. Cohn, "Frequency swept measurements of coherent diffraction patterns," *Appl. Opt.* **37**, 8131–8133 (1998).
18. R. R. Read, J. L. Shanks, and S. Treitel, "Two dimensional recursive filtering," in *Picture Processing and Digital Filtering*, Vol. 6 of Topics in Applied Physics, T. S. Huang, ed. (Springer-Verlag, Berlin, 1979), pp. 131–176.
19. J. S. Lim, "Image restoration," in *Two-Dimensional Signal- and Image Processing* (Prentice-Hall, Englewood Cliffs, N.J., 1990), pp. 524–588.
20. A. V. Oppenheim and R. W. Shafer, *Discrete-Time Signal Processing* (Prentice-Hall, Englewood Cliffs, N.J., 1989), p. 530.